Supporting Information for "Stress chatter on a fracture network reactivated by hydraulic fracturing"

Andres F. Peña Castro[1,†], Marco P. Roth[2,†], Alessandro Verdecchia[1], John Onwuemeka[1], Yajing Liu[1], Rebecca M. Harrington[2], Yong Zhang[3], Honn Kao[4]

[1]Department of Earth and Planetary Sciences, McGill University, Montréal, Québec, Canada

[2]Institute of Geology, Mineralogy and Geophysics, Ruhr University Bochum, Bochum, Germany

[3]School of Earth and Space Sciences, Peking University, China

[4]Pacific Geoscience Centre, Geological Survey of Canada, Sidney, British Columbia, Canada

[†]These authors contributed equally to this work.

Contents of this file

S1 Multi-station matched-filter detection

Each 6-second template waveform begins 0.1 s before the P-arrival and contains separate P- and S-wave phase recordings on three components. Table S2 lists the origin time and the number of secondary detections for each of the templates. Before performing the MMF detection by cross-correlation across all stations in a time step of 0.025 s, we re-sample the template waveforms to 40 sps and apply a bandpass filter of 2-10 Hz. Station NBC4 was not used in some cases due to multiple data gaps in the 20-day period. Detections are declared when the summed correlation function exceeds a pre-set threshold, empirically chosen to be 8 times the Median Absolute Deviation (MAD) of the day-long CC sum.

If at least one channel exhibits a CC value of at least 0.4 with respect to the template, a possible detection is declared. Detections for which an analyst observes visible P- and/or S-waves at the station for which the detection is generated are retained. We located detections that generate picks on at least four stations, and assume events with detections on fewer stations are co-located with templates.

S2 Seismicity relocation

Both approaches (*HypoDD* and *GrowClust*) use the reference *NonLinLoc* (Lomax et al., 2000) initial locations, differential travel times, and cross-correlation coefficients to simultaneously group and relocate events within similar clusters (Waldhauser & Ellsworth, 2000; Trugman & Shearer, 2017). We use slightly different settings for each approach. The *HypoDD*(Waldhauser & Ellsworth, 2000) relocation algorithm uses differential travel times from cross-correlation of event waveforms using 2.5 second time windows starting 1 sec prior to and 1.5 sec after the phase arrival pick, with waveforms bandpass filtered

between 2 and 15 Hz. We retain differential travel times between events with a cross-correlation coefficient of 0.6 or higher. Initial iterations weight the catalog phase picks relative to cross-correlation differential travel times by a ratio of 100:1 to constrain absolute hypocentral locations. The subsequent 20 iterations weight catalog phase picks to differential phase picks by a ratio of 1:100 to reduce the relative relocation error within the cluster. Following the relocation calculation, location error is then estimated by a bootstrap random replacement scheme with 100 trials. The above settings lead to a total number of 68 relocated events with relative horizontal and vertical location error of 60 and 80 m, respectively.

For the *GrowClust* (Trugman & Shearer, 2017) algorithm, we determine differential travel times using data cut by time windows starting 1.0 sec before and 1.5 sec after the P-arrival pick, and 1.0 sec before and 2.5 sec after the S-wave arrival pick. We apply a bandpass filter of 2-10 Hz prior to cross-correlation value calculation, and require a minimum of eight phases with cross-correlation coefficient values > 0.6 and an RMS cut-off of 0.3 s. The above parameter settings lead to 59 relocated events, with mean horizontal and vertical location error of 520 m and 450 m, respectively, a 10-fold reduction compared to the initial location errors. The relocations obtained with *GrowClust* are shown in Figure S3. Both relocation algorithms highlight similar features, where RMS travel-time residuals are lower for HypoDD than GrowClust (Figure S4).

S3 Earthquake source parameter estimation

We first estimate the station averaged M_0 and f_c values by fitting individual spectra using the Brune model (Brune, 1970) for events with signal to noise ratio SNR > 2 in the

frequency band of 0.1 - 45 Hz using magnitude dependent time windows (4 s for M $>$ 4 events, and 2 s for M $<$ 4 events) and a multi-taper spectral estimation(Prieto et al., 2007, 2009). The SNR is calculated using noise spectra estimated from time windows of identical length to the signal spectra. We first constrain the seismic moment (M_0) and spectral corner frequency values (f_c) using a least squares fit to the following equation(Brune, 1970; Boatwright, 1978):

$$\Omega(f) = \frac{\Omega_0 e^{-(\frac{\pi f t}{Q})}}{(1 + (\frac{f}{f_c})^{\gamma n})^{1/\gamma}}, \tag{1}$$

where Ω_0 is the long-period spectra amplitude, Q is the seismic quality factor, t is the travel time, n is the spectral falloff rate, and γ is the corner shape determinant (e.g., (Abercrombie, 1995)). We then use the fitted Ω_0 and f_c values to determine values of moment and static stress drop ($\Delta\sigma$) for estimating average fault area and slip for the Coulomb stress calculation. The moment calculation is computed with

$$M_0 = \frac{4\pi\rho\beta^3\Omega_0 R}{U_{\phi\theta}}, \tag{2}$$

where ρ is the average curstal density (2.7 kg/m^3), R is the hypocentral distance, β is the depth dependent shear wave velocity (Table S1), and $U_{\phi\theta}$ is the average radiation pattern for S-waves (Eshelby, 1957).

We can relate the static stress drop for a circular, two-dimensional fault to the scalar moment using the following equation (Burridge & Knopoff, 1964):

$$M_0 = \frac{16}{7}\Delta\sigma a^3 \tag{3}$$

where a is the fault radius. We then relate f_c to a using the following relationship (Madariaga, 1976):

$$a = \frac{0.32\beta}{f_c}. \tag{4}$$

Figures S5 and S6 show the spectra fitting of the mainshock and the stress drop spectra, respectively. Table S3 lists the corner frequency and stress drop values obtained through the fitting procedure described above.

We use the probabilistic earthquake source inversion framework *Grond* (Heimann et al., 2018) to compute full moment tensor solutions. We start by computing Greens Functions (GFs) with Qseis (Wang, 1999) over a 100×100×15 km^3 volume with step-length of 200 m using the velocity model in Table S1. We then cut event waveforms over 0.8-second time-windows starting 0.05 sec before the analyst-picked phase arrivals. The algorithm then simulates synthetic waveforms from a set of 18,000-30,000 trial models (centroid and moment tensors) within the GF volume and fits each synthetic waveform with the observed data for both P- and S-waves in both frequency and time domains, as well as waveform envelopes. The optimal moment tensor and centroid is determined based on a Bayesian bootstrap optimization, which enables full probabilistic bootstrapping of optimization solutions (Heimann et al., 2018). The bootstrapping optimization technique also provides an uncertainty estimation that typically decreases with increasing iterations.

Given that the source mechanism could potentially involve significant non-double couple components due to fluid injection and rupture on adjacent and/or intersecting fault structures, we estimate full moment tensor solutions (including isotropic, compensated-

linear vector dipole, and double couple components) to try and identify possible source complexity. We obtain robust moment tensor solutions for one foreshock, the mainshock, and 3 aftershocks (Tables S4 and S5). The focal mechanism and centroid solutions are consistent with the general trend of the relocated seismicity, and suggest a thrust fault solution for the mainshock, and predominantly strike-slip solutions for aftershocks in the sedimentary layers. Both types of solutions are consistent with roughly optimally oriented faults in the regional stress field. All estimated centroids lie within less than 300 m of their corresponding relocated hypocenters, and provide an independent validation of the hypocenter relocation.

S4 Poroelastic stress model The governing equations of linear poroelasticity can be written as (Wang & Kümpel, 2003):

$$G\nabla\mu + \frac{G}{1-2\nu}\nabla\epsilon - \alpha\Delta p = f(x,t) \tag{5}$$

$$\frac{1}{M}\frac{\partial p}{\partial t} + \alpha\frac{\partial \epsilon}{\partial t} - \nabla\cdot(\frac{\kappa}{\eta}\nabla p) = q(x,t) \tag{6}$$

where μ is the displacement vector, p is the excess pore pressure, $\epsilon = \nabla\cdot\mu$ is the volumetric strain, G is the shear modulus, ν is Poisson's ratio under drained conditions, α is the Biot coefficient, M is the Biot modulus, κ is the matrix permeability, η is dynamic viscosity of the fluid, f is the body force per unit volume acting on the solid matrix, and q is the fluid volume injection rate (fluid source density).

The stress-strain relation of the solid matrix when pore fluid p is under pressure is given by

$$\sigma_{ij} = \frac{2G\nu}{1-2\nu}\epsilon\delta_{ij} + 2G\epsilon_{ij} - \alpha p\delta_{ij} \tag{7}$$

where δ_{ij} is the Kronecker delta.

S5 Finite slip inversion

We invert the finite slip distribution of the M_L 4.5 mainshock, by assuming slip on either of the two conjugated fault planes from the mainshock focal mechanism solution (Table S4) (Zhang et al., 2012; Wang et al., 2017). The 4.2 km by 4.2 km fault plane is equally divided into $21 \times 21 = 421$ sub-faults (grid size 0.2 km) (Figure S10). The hypocenter is located at the center of the fault. Slip inversion uses the 1D velocity model as in Table S1. Velocity waveforms are integrated into displacement and band-pass filtered 0.05-1 Hz. Due to the small magnitude of the mainshock, we assume a maximum rupture velocity of 2.5 km/s and a rupture duration of 3 s for the inversion. Slip inversion results and corresponding Coulomb stress change are shown in Fig. S10. A higher resolution 3D velocity model and/or closer station-source distances would lead to a better constrained slip inversion for this relatively low magnitude event.

Figures

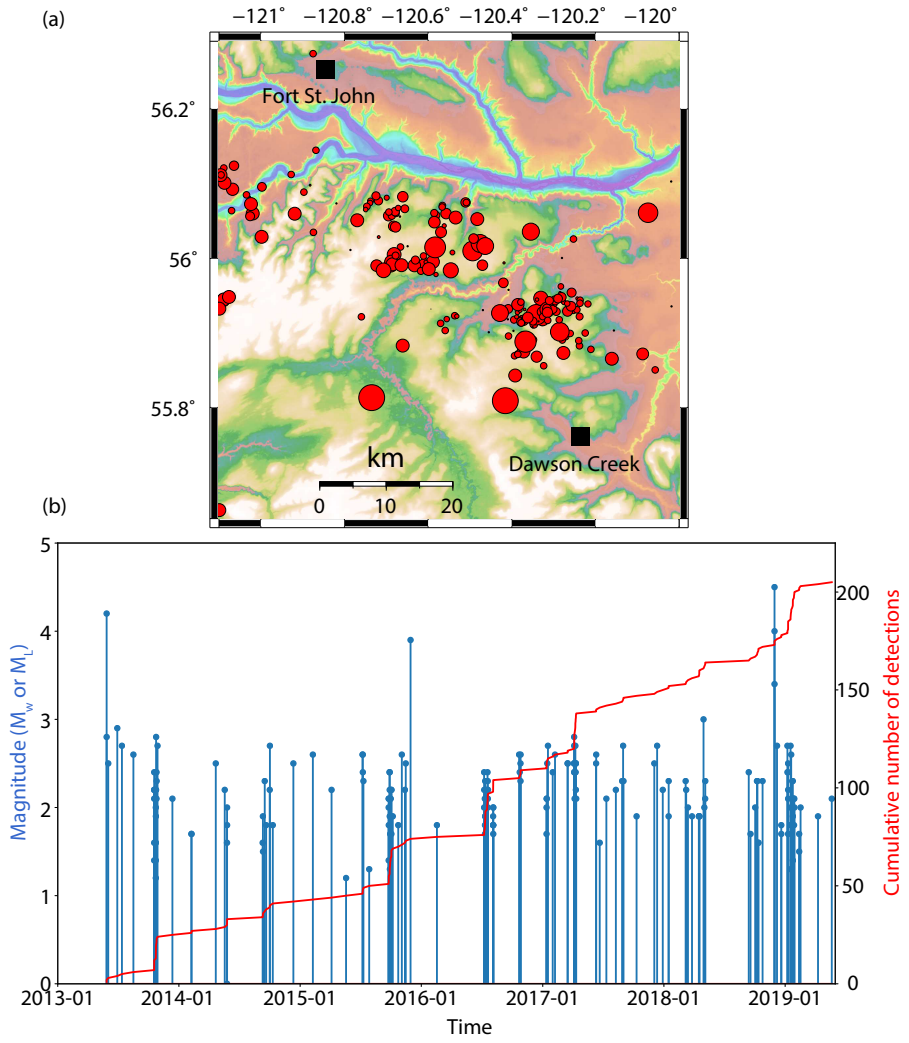

Figure S1. (a) Map overview of the seismicity reported by NRCan (*Natural Resources Canada Earthquakes Canada, GSC, Earthquake Search (On-line Bulletin)*, n.d.) from 2013 until June 2019 on the Dawson Septimus area. (b) Magnitude vs time (blue dots) of the same earthquakes shown in (a); red line indicates the cumulative number of earthquakes.

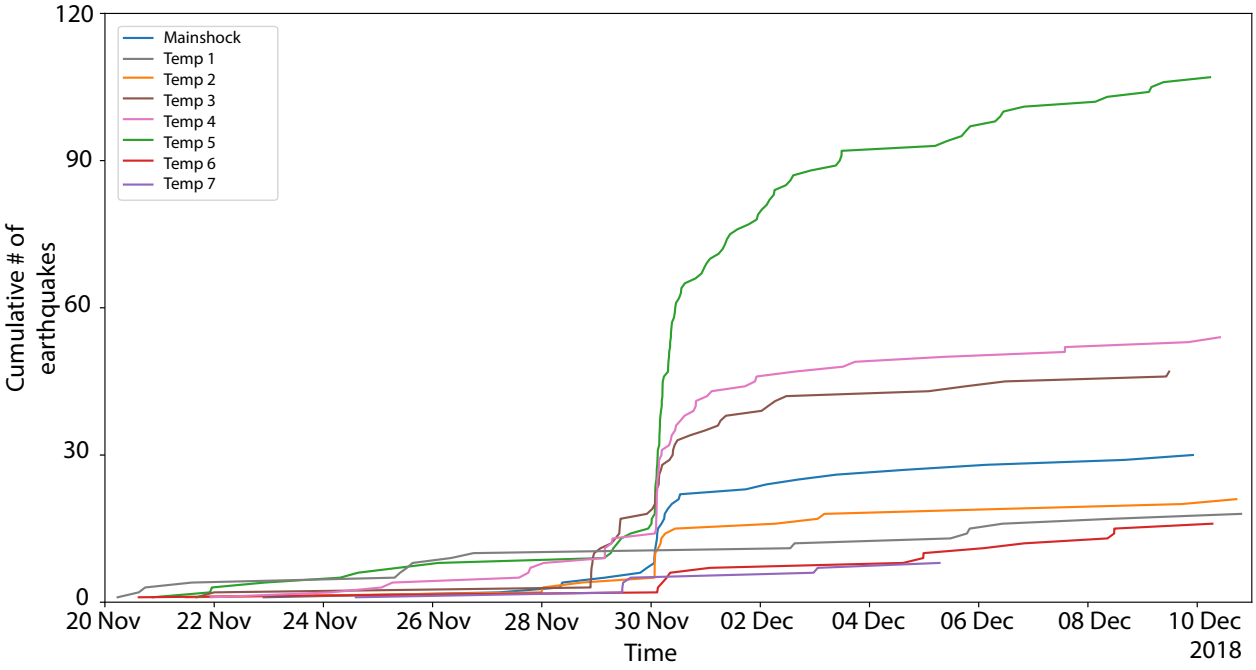

Figure S2. Number of earthquakes detected by each of the templates (Table S2) from Nov 20 until Dec 11. Templates 3 (brown line) and 4 (pink line) (the strongest aftershocks), and 5 detected a total of 178 more events than the Mainshock template (blue line).

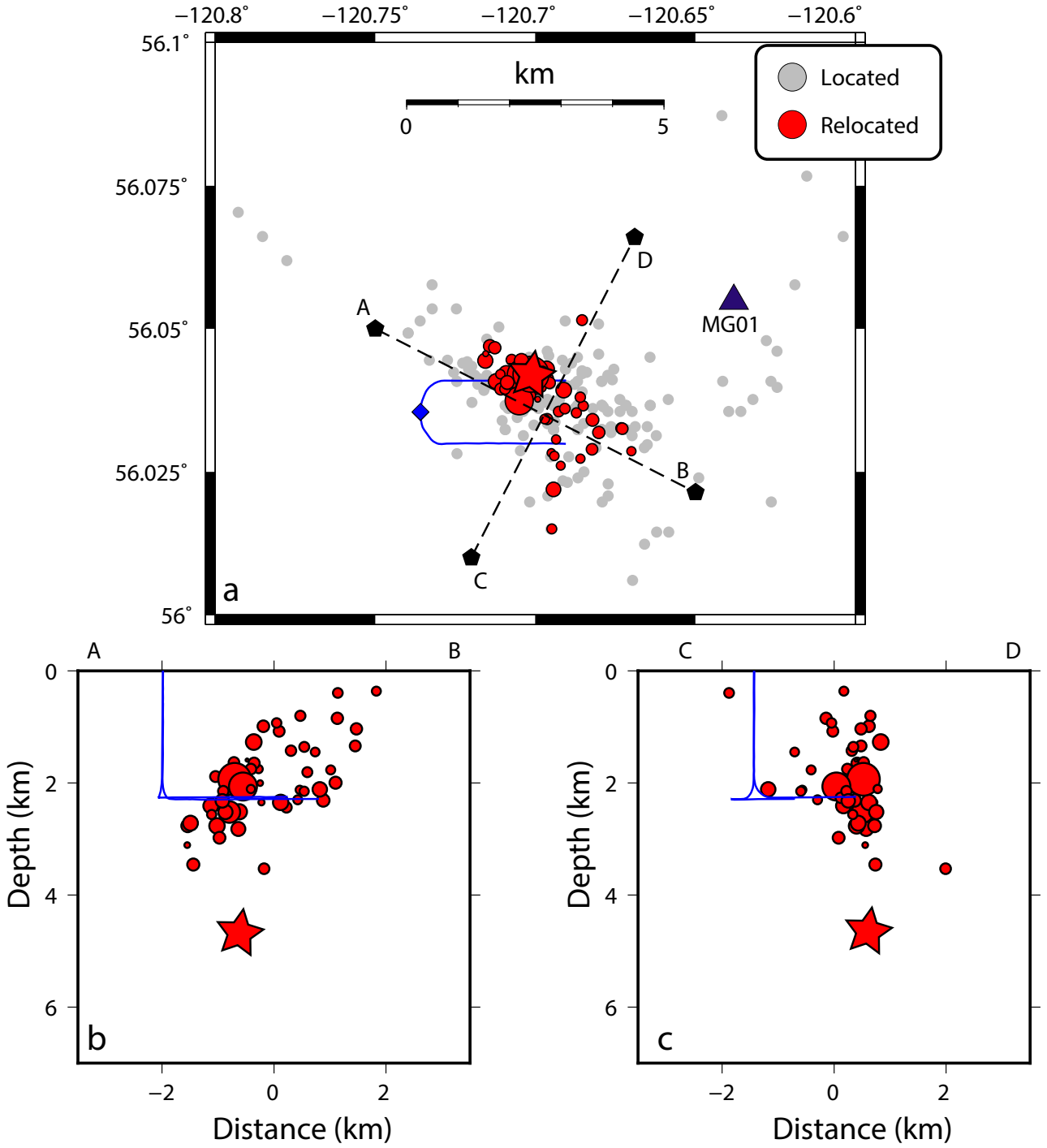

Figure S3. (a) Map view of earthquakes relocated using *GrowClust* (red circles) and initial locatations determined with *NonLinLoc* (gray circles). (b) and (c) are relocated earthquake profiles (same as Figure 3)). Red star shows the Mainshock relocation.

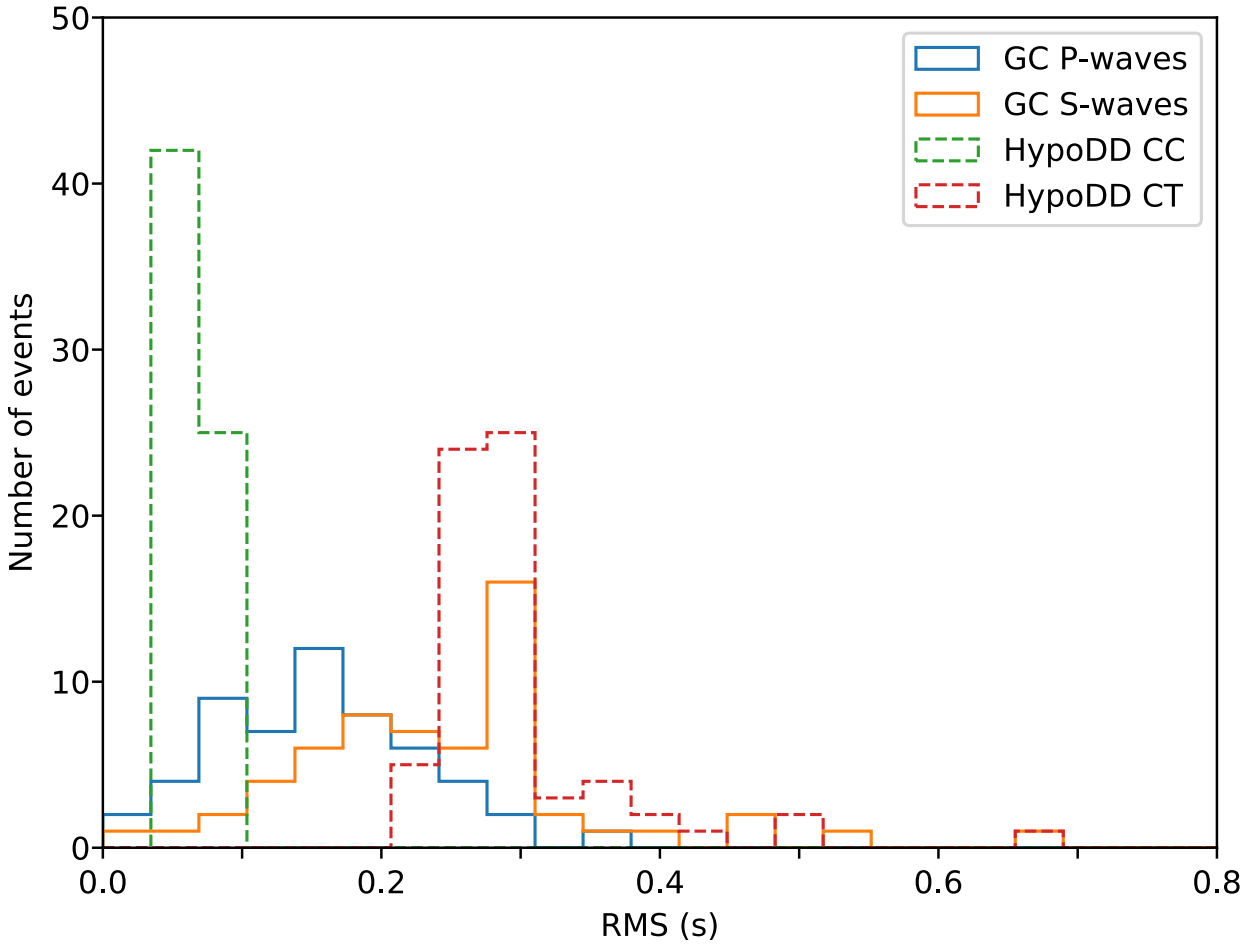

Figure S4. Root-Mean-Square (RMS) residual differential times for each of the relocation methods (*GrowClust* and *HypoDD*). *Growclust* outputs RMS for P- and S- waves separately while *HypoDD* shows the RMS for the iteration of the catalogue (CT) and the cross-correlation procedure (CC). RMS relocation values are lower for *HypoDD* solutions, as indicated by the green dashed line.

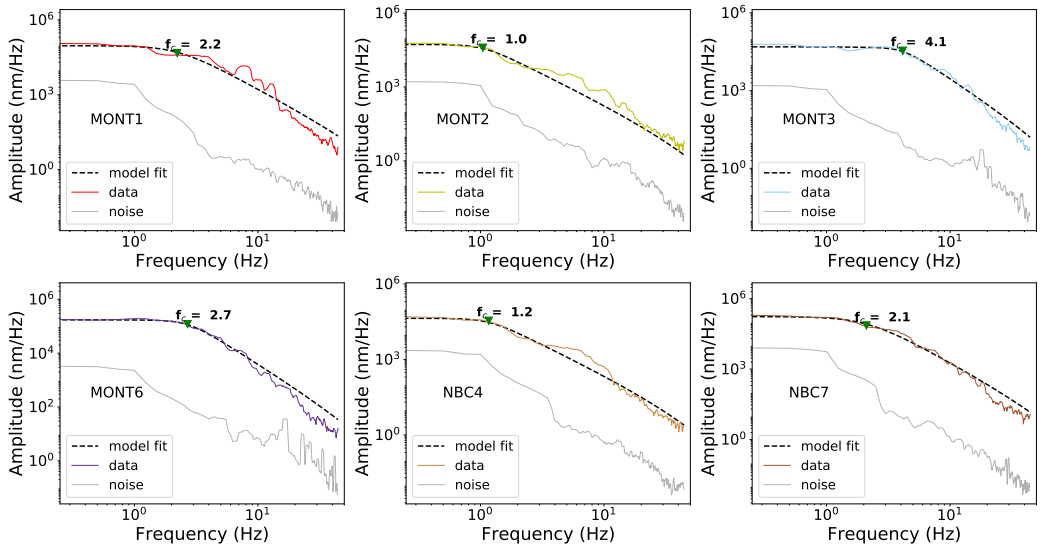

Figure S5. Single-spectrum fit of the windowed waveform data of the mainshock for various stations. Dotted-black and gray lines represent the model fit of the mainshock spectra (colored lines) and the noise spectra, respectively. Corner frequency estimates from each fit at an individual station are indicated by green triangles.

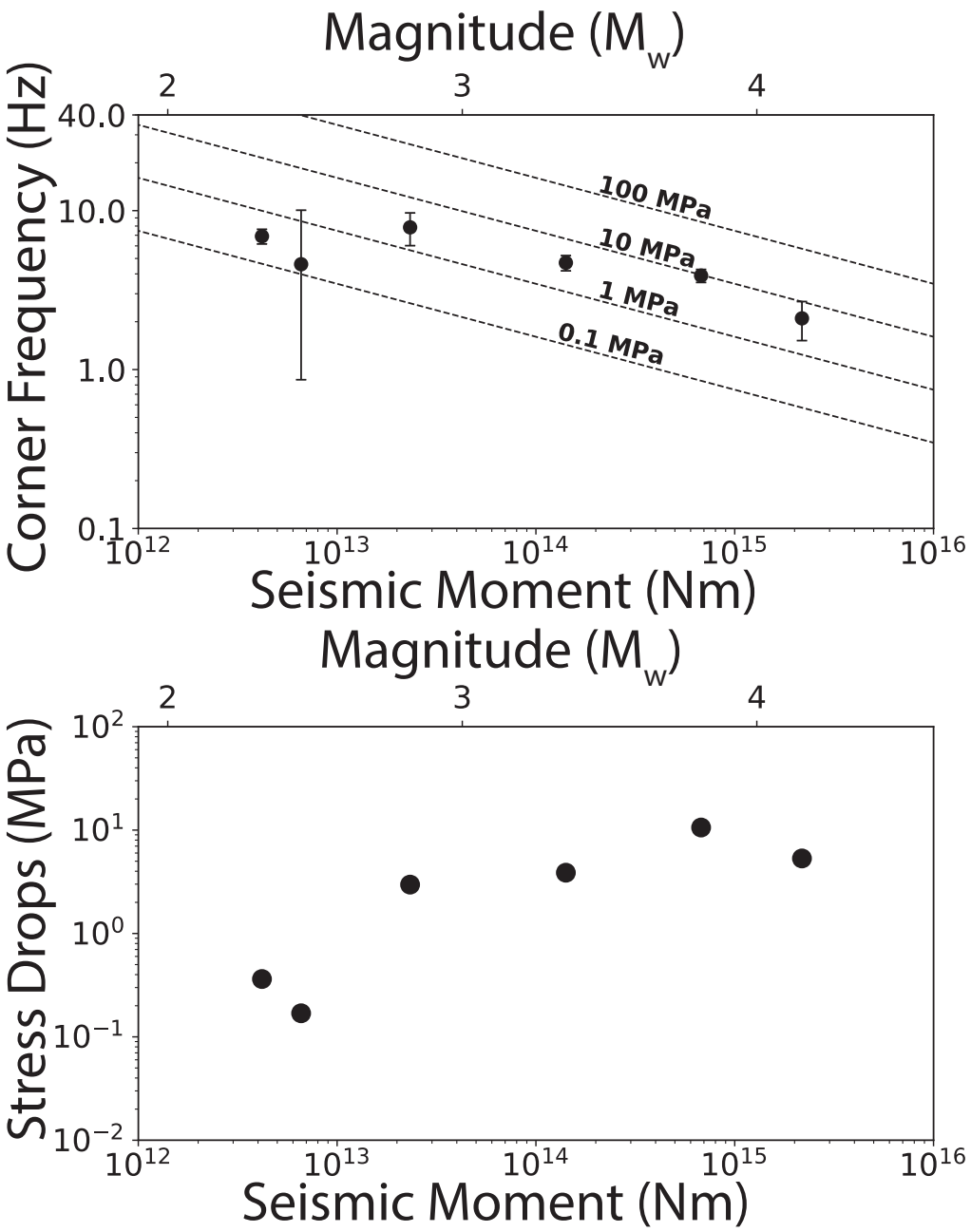

Figure S6. Corner frequency versus seismic moment. The black dots represent corner frequency estimates for one foreshock, the mainshock, and four aftershocks. Dashed lines show constant stress drop lines computed assuming a shear wave velocity of 3.3 km/s. Error bars indicate 95% confidence intervals of each event corner frequency estimate.

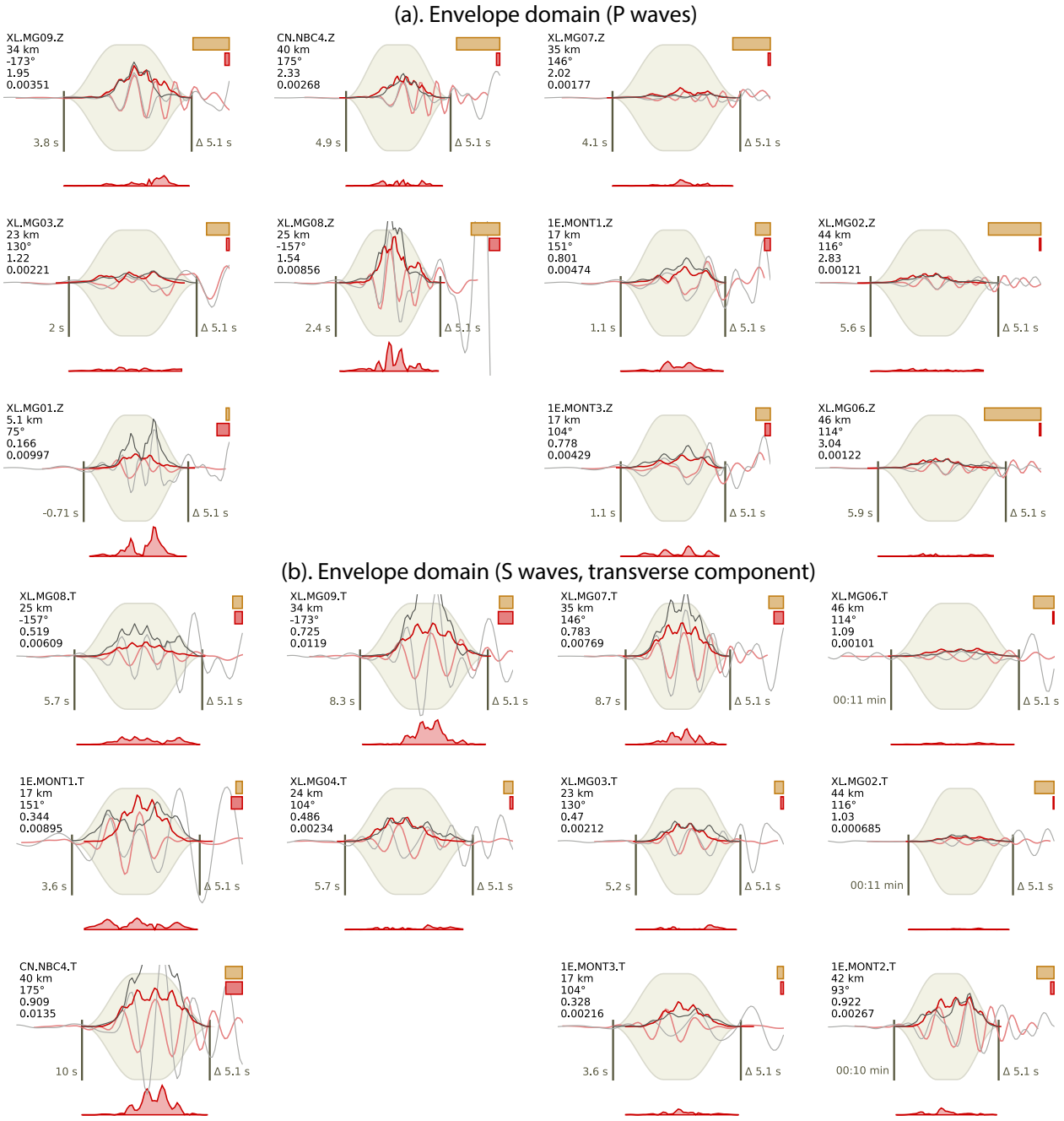
(a). Envelope domain (P waves)
XL.MG09.Z
34 km
-173°
1.95
0.00351
3.8 s
Δ 5.1 s
CN.NBC4.Z
40 km
175°
2.33
0.00268
4.9 s
Δ 5.1 s
XL.MG07.Z
35 km
146°
2.02
0.00177
4.1 s
Δ 5.1 s
XL.MG03.Z
23 km
130°
1.22
0.00221
2 s
Δ 5.1 s
XL.MG08.Z
25 km
-157°
1.54
0.00856
2.4 s
Δ 5.1 s
1E.MONT1.Z
17 km
151°
0.801
0.00474
1.1 s
Δ 5.1 s
XL.MG02.Z
44 km
116°
2.83
0.00121
5.6 s
Δ 5.1 s
XL.MG01.Z
5.1 km
75°
0.166
0.00997
-0.71 s
Δ 5.1 s
1E.MONT3.Z
17 km
104°
0.778
0.00429
1.1 s
Δ 5.1 s
XL.MG06.Z
46 km
114°
3.04
0.00122
5.9 s
Δ 5.1 s
(b). Envelope domain (S waves, transverse component)
XL.MG08.T
25 km
-157°
0.519
0.00609
5.7 s
Δ 5.1 s
XL.MG09.T
34 km
-173°
0.725
0.0119
8.3 s
Δ 5.1 s
XL.MG07.T
35 km
146°
0.783
0.00769
8.7 s
Δ 5.1 s
XL.MG06.T
46 km
114°
1.09
0.00101
00:11 min
Δ 5.1 s
1E.MONT1.T
17 km
151°
0.344
0.00895
3.6 s
Δ 5.1 s
XL.MG04.T
24 km
104°
0.486
0.00234
5.7 s
Δ 5.1 s
XL.MG03.T
23 km
130°
0.47
0.00212
5.2 s
Δ 5.1 s
XL.MG02.T
44 km
116°
1.03
0.000685
00:11 min
Δ 5.1 s
CN.NBC4.T
40 km
175°
0.909
0.0135
10 s
Δ 5.1 s
1E.MONT3.T
17 km
104°
0.328
0.00216
3.6 s
Δ 5.1 s
1E.MONT2.T
42 km
93°
0.922
0.00267
00:10 min
Δ 5.1 s

(c). Frequency domain (P waves)

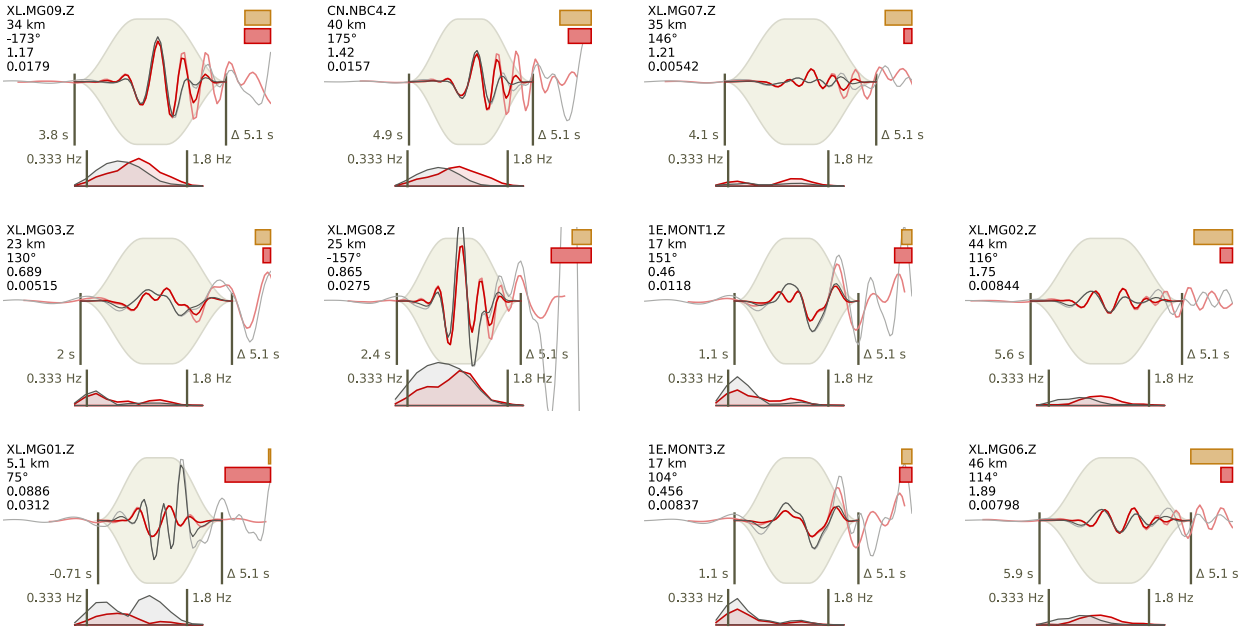

(d). Frequency domain (S waves, transverse component)

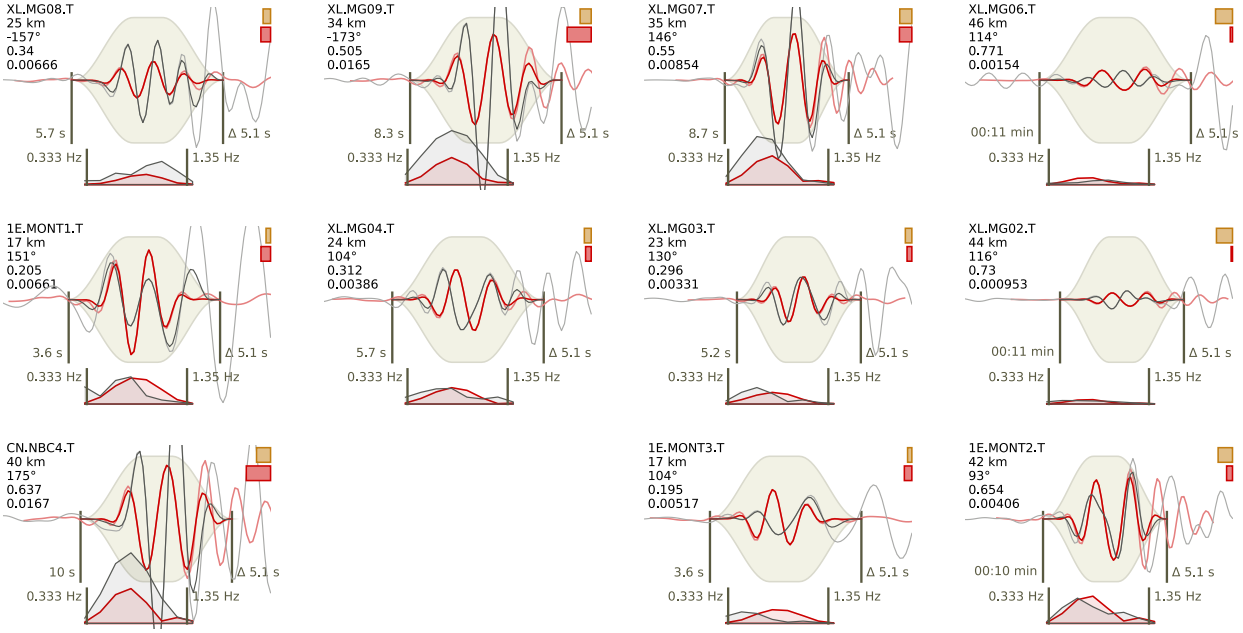

(e). Time domain (P waves)

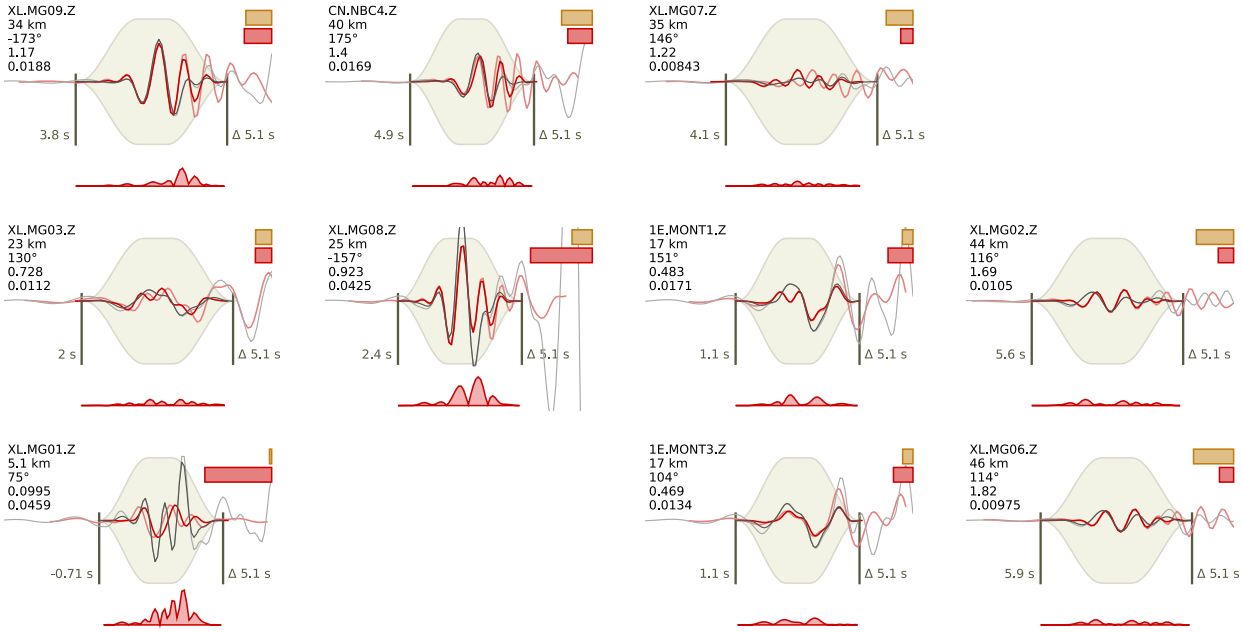

(f). Time domain (S waves, transverse component)

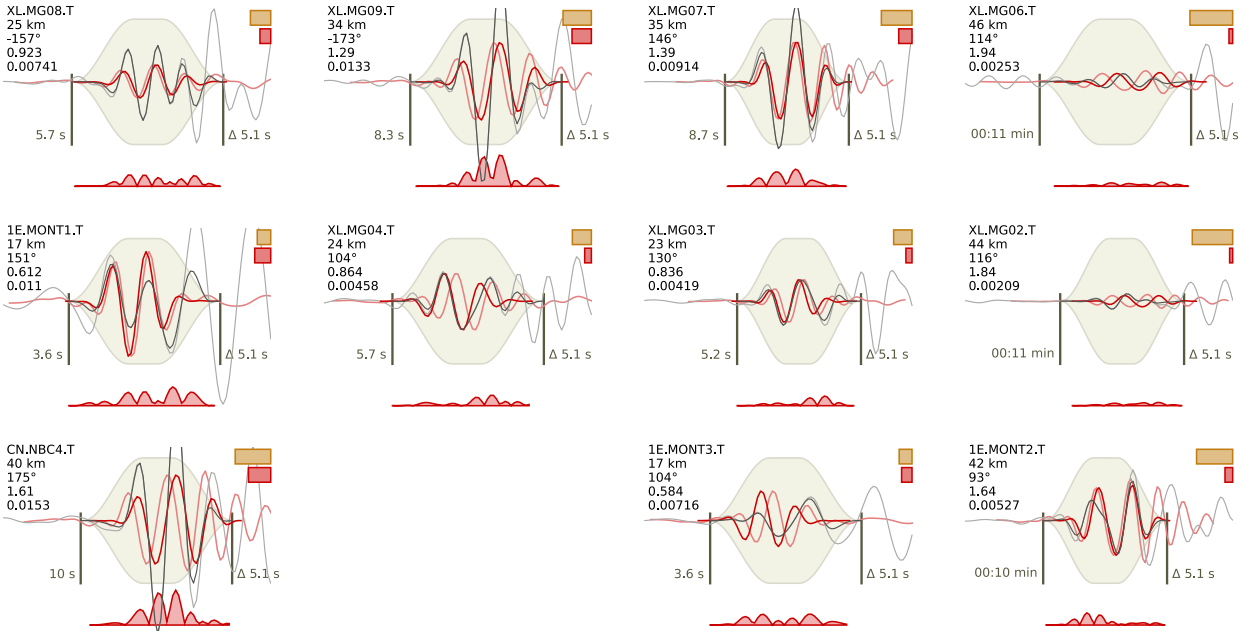

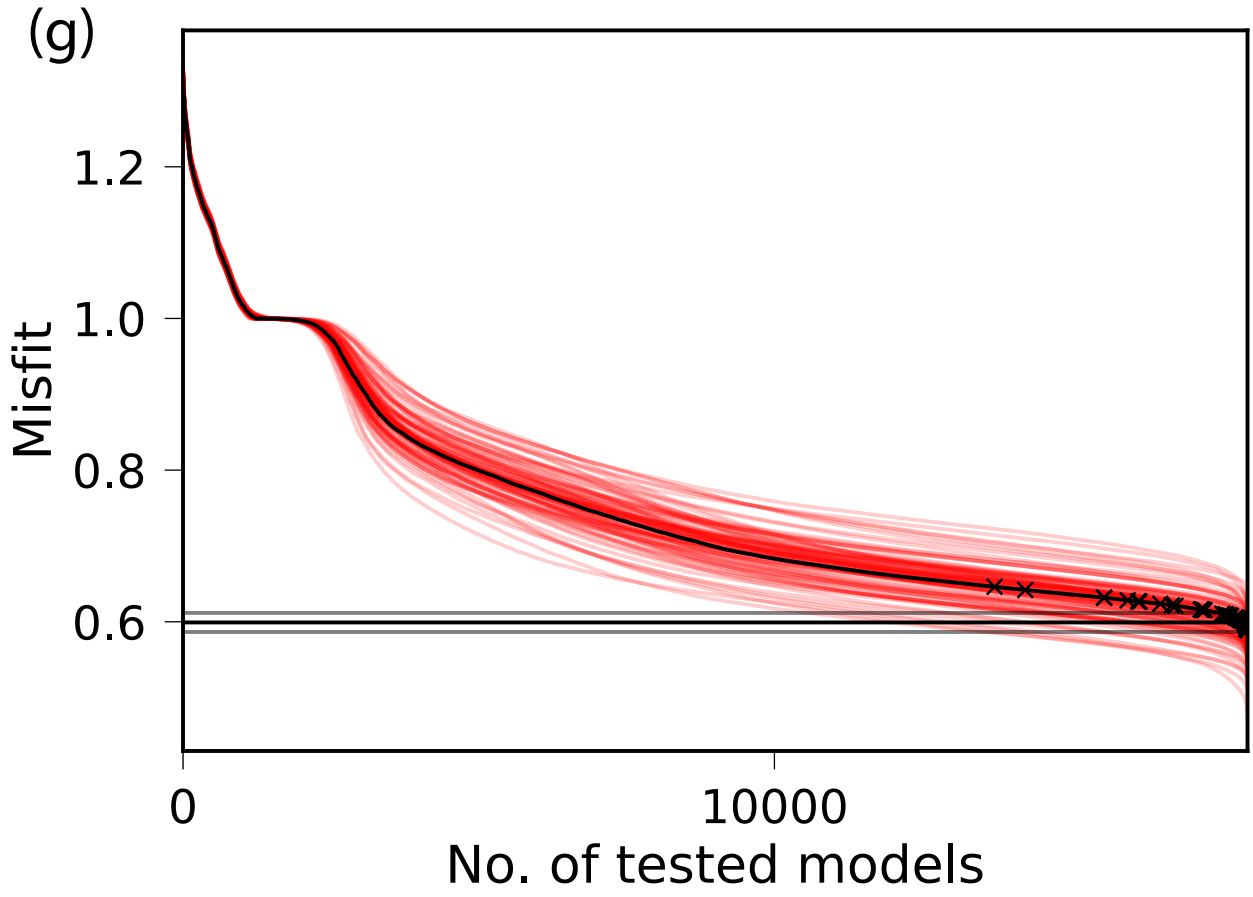

Figure S7. Waveform fitting for the M_L 4.5 mainshock for P-wave and S-wave in (a-b) envelope, (c-d) frequency domain, and (e-f) time domain. Black and red traces represent observed and synthetic waveforms respectively. Light and and strong colors indicate tapered and untapered data, respectively. Light red traces are unshifted, dark red lines indicate the final fits. Residuals are given by the red trace at the bottom of each graph. Relative weighting factor (balancing weights during inversion) and relative residuals are indicated by yellow and red bars, respectively. Network, station, and component; station-epicenter distance; source-to-station azimuth; solution weight factor; and normalized residual are indicated to the right of each plot in (a-f). The value on the left-hand side (of each single panel showing an inversion) is the onset time with respect to the event origin; the time interval between the two black marker lines is indicated on the right. The global misfit is shown in (g). `January 27, 2020, 3:34am`

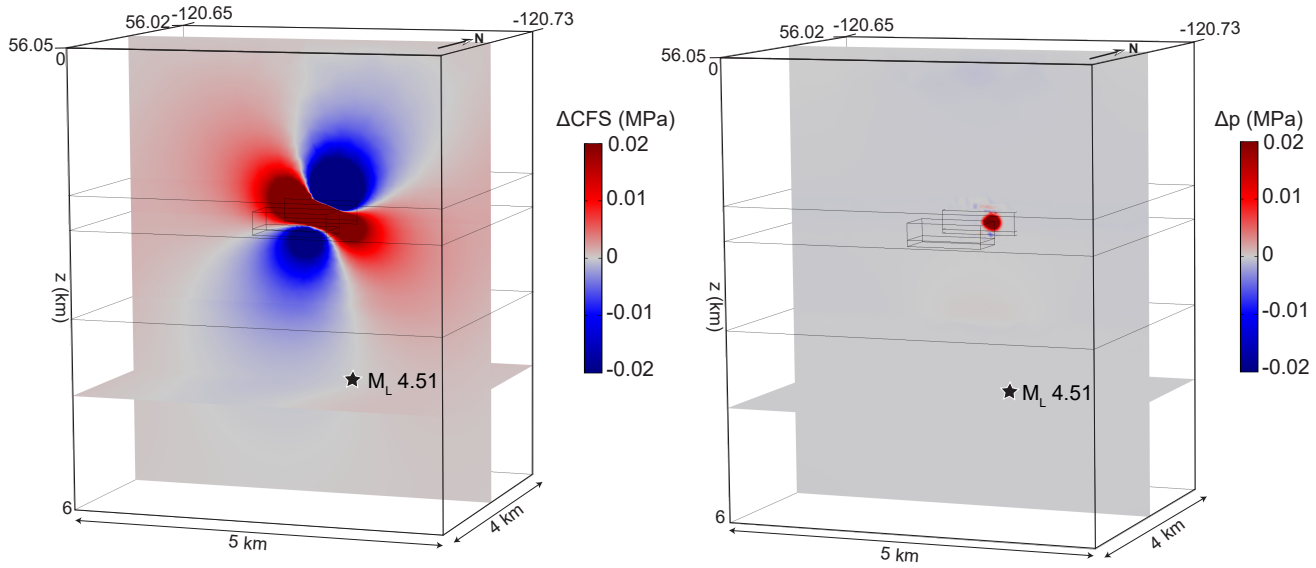

Figure S8. Coulomb stress (ΔCFS) (left) and pore pressure changes (Δp) (right) due to fluid injections calculated on the geometry and kinematics of the M_L 4.5 mainshock just before the occurrence of the earthquake using a poroelasic model without high-permeability fault zones. At the mainshock location, we calculate no pore pressure changes (right), and ΔCFS of 0.00015 MPa (left). Permeability values for the different layers are listed in Table 5

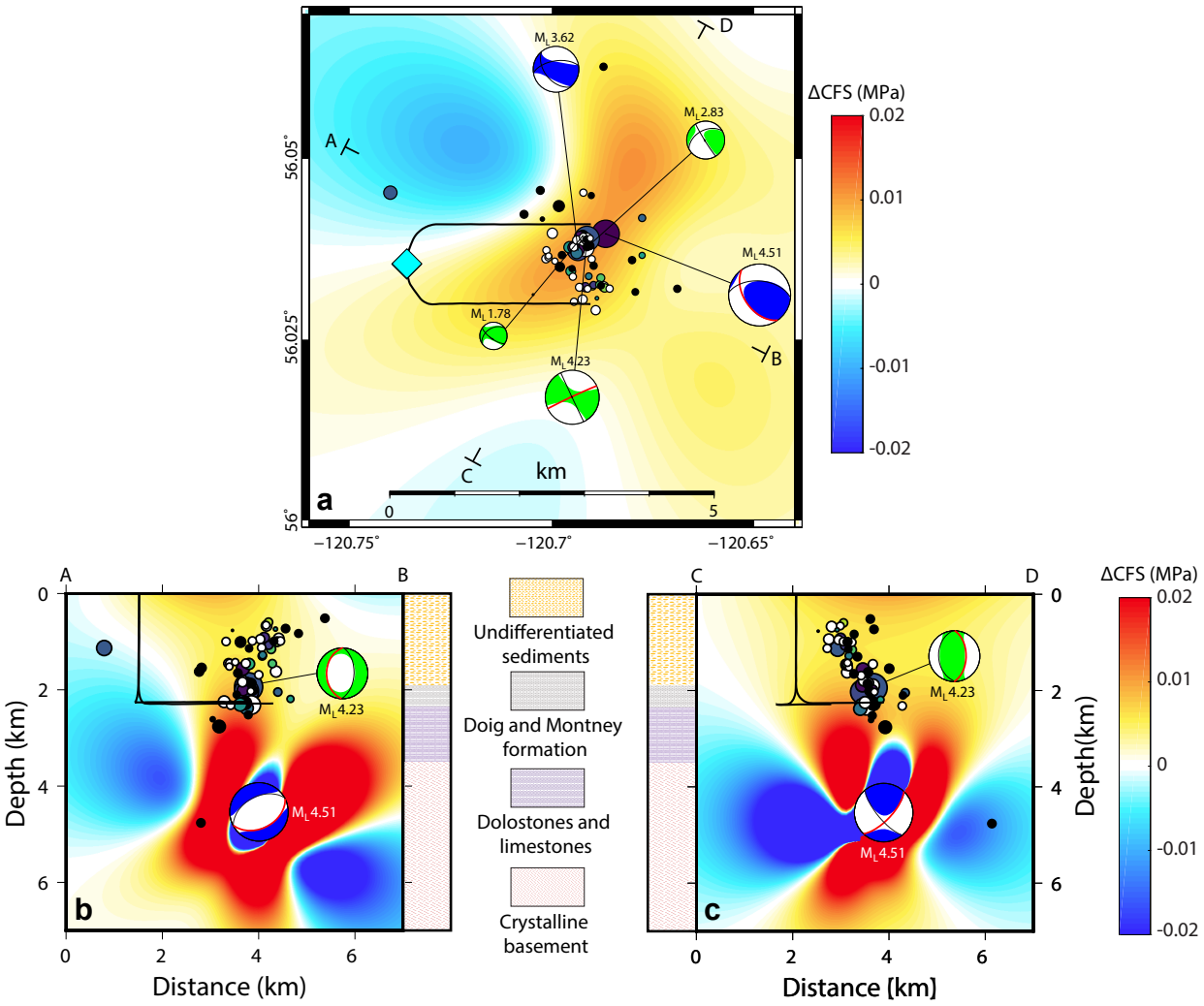

Figure S9. Coulomb stress changes (ΔCFS) calculated based on the geometry and kinematics of the M_L 4.2 aftershock (green focal mechanism, red line) inferred from the solution of the north-east dipping fault plane (blue focal mechanism, red line). ΔCFS are shown on (a) map view at 1.9 km calculation depth, and (b, c) on cross-section.

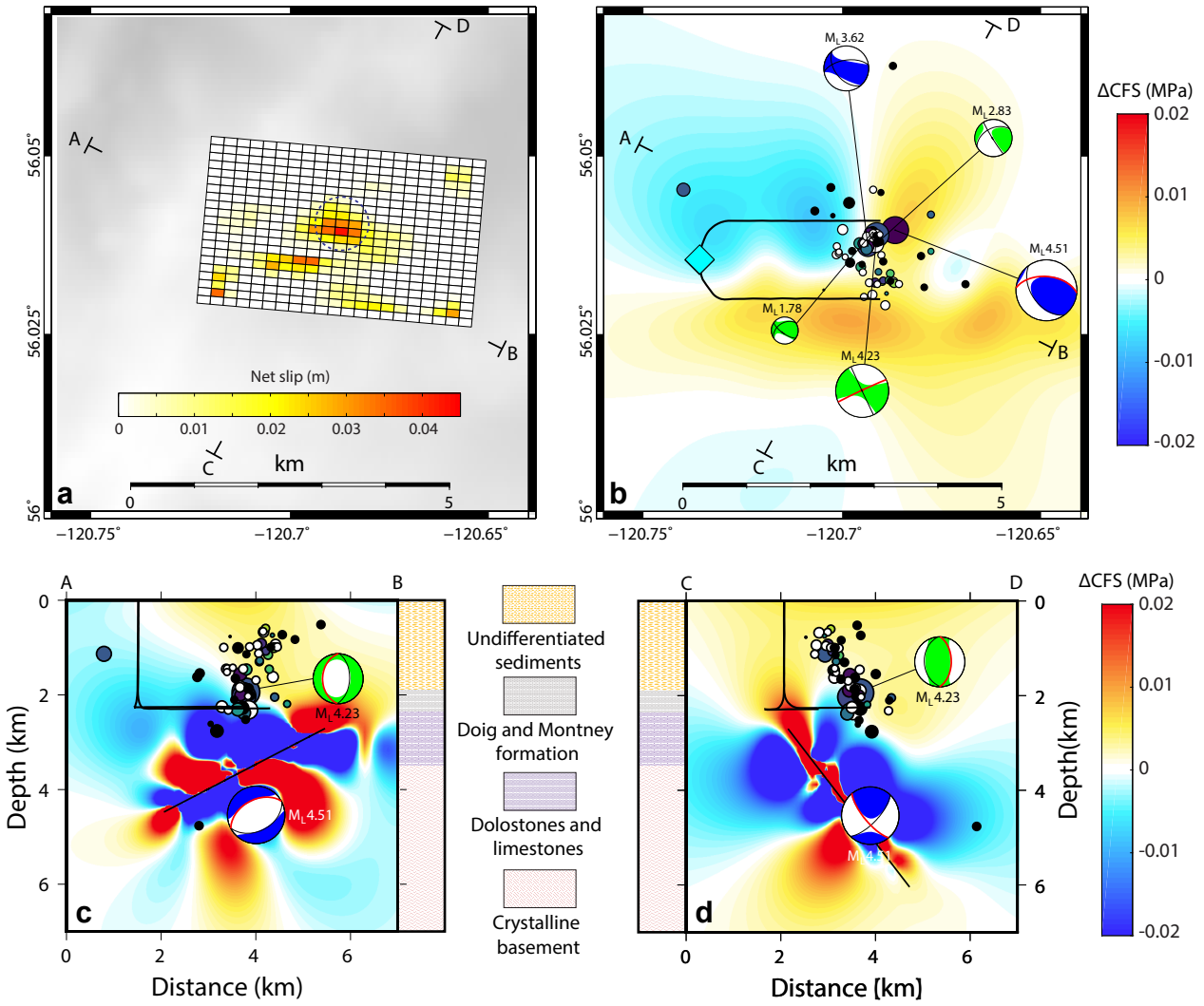

Figure S10. Coulomb stress changes (ΔCFS) calculated based on the geometry and kinematics of the M_L 4.2 aftershock (green focal mechanism, red line) inferred from the solution of the north-east dipping fault plane (blue focal mechanism, red line) calculated using a finite slip model based on full waveform inversion (a). ΔCFS is shown on (b) map view at 1.9 km calculation depth, and (c, d) on cross-section. The dashed circle in (a) represents the slip area adopted in the uniform slip model.

Tables

Depth to bottom of layer (km)	P-wave velocity (km/s)	S-wave velocity (km/s)
0.	2.5	1.07
1.	4.8	2.8
2.	5.5	3.2
4.	6.1	3.5
8.	6.2	3.6
25.	6.5	3.7
33.	8.045	4.48

Table S1. Velocity model used for *NonLinLoc* catalog location, *HypoDD* earthquake relative relocation calculation, and *Grond* Green's function database calculation, adapted from Crust1.0 (Laske et al., 2013) (for layers above 1 km) and from (Mahani et al., 2017) (for deeper layers).

.

Name	Date, Origin Time	Magnitude	# of Channels	# of Detections
Mainshock	11/30/2018, 01:27:05	4.5	45	30
Template 1	05/05/2018, 14:39:03	2.8	27	18
Template 2	11/30/2018, 01:34:41	1.5	20	21
Template 3	11/30/2018, 02:06:01	3.6	45	47
Template 4	11/30/2018, 02:15:00	4.2	45	54
Template 5	11/30/2018, 10:36:58	1.3	29	107
Template 6	11/30/2018, 11:30:27	2.0	39	16
Template 7	12/02/2018, 23:24:40	1.2	18	8

Table S2. Template earthquakes used in the Multi-station Matched Filter (MMF) enhanced catalog detection in the 20 days surrounding the M_L 4.5 mainshock. Events consist of the mainshock and six well-recorded aftershocks, as well as a well-recorded event located on a fault structure antithetic to the M_L 4.5 event.)

.

Event Origin time	Seismic moment (Nm)	Moment magnitude	Corner freq. (Hz)	Confidence intervals (Hz)	Stress drop (MPa)
2018-11-29T11:44:29	6.591295e+12	2.5	4.6	-3.74/+5.46	0.17
2018-11-30T01:27:07	2.178520e+15	4.2	2.1	-0.58/+0.58	5.32
2018-11-30T02:06:02	1.414627e+14	3.4	4.7	-0.52/+0.52	3.87
2018-11-30T02:15:01	6.774354e+14	3.8	3.9	-0.37/+0.37	10.6
2018-11-30T02:35:30	4.187790e+12	2.3	6.9	-0.73/+0.73	0.36
2018-12-07T13:49:26	2.328523e+13	2.8	7.85	-1.83/+1.83	2.97

Table S3. Source parameter estimation (corner frequency and stress drop values)

Origin Time	Lat(°)	Long(°)	Depth (km)	Strikes	Dips	Rakes
2018-11-30T01:26:36	56.0357	-120.7189	2.7	[125,236]	[71,43]	[129,28]
2018-11-30T01:27:07	56.0432	-120.7168	4.4	[274,144]	[52,49]	[54,127]
2018-11-30T02:06:02	56.0411	-120.6972	3.0	[261,140]	[59,49]	[49,138]
2018-11-30T02:15:01	56.0473	-120.6897	2.9	[245,155]	[88,89	[0,178]
2018-12-07T13:49:26	56.0453	-120.6973	2.5	[241,148]	[47,86]	[6,136]

Table S4. Fault planes solution from the focal mechanism solutions.

Origin Time	ISO (%)	CLVD (%)	DC (%)
2018-11-30T01:26:36	0.18	0.15	0.66
2018-11-30T01:27:07	0.02	0.24	0.74
2018-11-30T02:06:02	0.08	0.66	0.26
2018-11-30T02:15:01	0.08	0.42	0.50
2018-12-07T13:49:26	0.11	0.03	0.86

Table S5. Isotropic (ISO), compensated-Linear vector dipole (CLVD) and double-couple (DC) component for each of the events that focal mechanism was obtained.

Layer	Thickness[a] (km)	V_p (m/s)	V_s (m/s)	Density[b] (kg/m^3)	Porosity	k (m^2)	α
Undifferentiated sediments	1.9	4800	2740	2500	0.1	10^{-16}	0.6
Doig and Montney formation (shales)	0.45	4800	2740	2500	0.1	10^{-18}	0.8
Dolostones and limestones	1.15	5500	3200	2500	0.1	10^{-17}	0.5
Crystalline basement	2.5	6100	3500	2790	0.05	10^{-19}	0.4

Table S6. Elastic and hydrological parameters used in the poroelastic stress model. [a]Data from the BCOGC (*British Columbia Oil and Gas Comission. Last accessed 2019/09/30*, 2019). [b]Data from Crust 1.0 (Laske et al., 2013)

Dynamic viscosity	0.28×10^{-3} Pa s
Density	1000 kg/m^3
Compressibility	4.6×10^{-10} Pa^{-1}

Table S7. Properties of injected fluids used in the poroelastic stress model.

References

Abercrombie, R. E. (1995). Earthquake source scaling relationships from -1 to 5 ml using seismograms recorded at 2.5-km depth. *Journal of Geophysical Research: Solid Earth*, *100*(B12), 24015–24036.

Boatwright, J. (1978). Detailed spectral analysis of two small New York State earthquakes. *Bulletin of the Seismological Society of America*, *68*(4), 1117–1131.

British Columbia Oil and Gas Comission. Last accessed 2019/09/30. (2019). Retrieved 2019-09-30, from `https://www.bcogc.ca/`

Brune, J. N. (1970). Tectonic stress and the spectra of seismic shear waves from earthquakes. *Journal of Geophysical Research*, *75*(26), 4997–5009.

Burridge, R., & Knopoff, L. (1964). Body force equivalents for seismic dislocations. *Bulletin of the Seismological Society of America*, *54*(6A), 1875–1888.

Eshelby, J. D. (1957). The determination of the elastic field of an ellipsoidal inclusion, and related problems. *Proceedings of the Royal Society of London. Series A. Mathematical and Physical Sciences*, *241*(1226), 376–396.

Heimann, S., Isken, M., Kühn, D., Sudhaus, H., Steinberg, A., Vasyura-Bathke, H., ... Dahm, T. (2018). *Grond - A probabilistic earthquake source inversion framework.* Retrieved 2018-08-27, from `http://pyrocko.org/grond/docs/current/` doi: 10.5880/GFZ.2.1.2018.003

Laske, G., Masters, G., Ma, Z., & Pasyanos, M. (2013). Update on crust1. 0—a 1-degree global model of earth's crust. In *Geophys. res. abstr* (Vol. 15, p. 2658).

Lomax, A., Virieux, J., Volant, P., & Berge-Thierry, C. (2000). Probabilistic earthquake location in 3D and layered models. In *Advances in seismic event location* (pp. 101–134). Springer.

Madariaga, R. (1976). Dynamics of an expanding circular fault. *Bulletin of the Seismological Society of America*, *66*(3), 639–666.

Mahani, A. B., Schultz, R., Kao, H., Walker, D., Johnson, J., & Salas, C. (2017). Fluid injection and seismic activity in the Northern Montney Play, British Columbia, Canada, with special reference to the 17 August 2015 Mw 4.6 induced earthquake. *Bulletin of the Seismological Society of America*, *107*(2), 542-552. doi: 10.1785/0120160175

Natural Resources Canada Earthquakes Canada, GSC, Earthquake Search (On-line Bulletin). (n.d.).

Prieto, G., Parker, R., Thomson, D., Vernon, F., & Graham, R. (2007). Reducing the bias of multitaper spectrum estimates. *Geophysical Journal International*, *171*(3), 1269–1281.

Prieto, G., Parker, R., & Vernon III, F. (2009). A Fortran 90 library for multitaper spectrum analysis. *Computers & Geosciences*, *35*(8), 1701–1710.

Trugman, D. T., & Shearer, P. M. (2017). Growclust: A hierarchical clustering algorithm for relative earthquake relocation, with application to the Spanish Springs and Sheldon, Nevada, earthquake sequences. *Seismological Research Letters*, *88*(2A), 379–391.

Waldhauser, F., & Ellsworth, W. L. (2000). A double-difference earthquake location algorithm: Method and application to the northern Hayward fault, California. *Bulletin of the Seismological Society of America*, *90*(6), 1353–1368.

Wang, R. (1999). A simple orthonormalization method for stable and efficient computation of green's functions. *Bulletin of the Seismological Society of America*, *89*(3), 733–741.

Wang, R., Heimann, S., Zhang, Y., Wang, H., & Dahm, T. (2017). Complete synthetic seismograms based on a spherical self-gravitating earth model with an atmosphere–ocean–mantle–

core structure. *Geophysical Journal International*, *210*(3), 1739–1764.

Wang, R., & Kümpel, H.-J. (2003). Poroelasticity: Efficient modeling of strongly coupled, slow deformation processes in a multilayered half-space. *Geophysics*, *68*(2), 705–717.

Zhang, Y., Feng, W., Chen, Y., Xu, L., Li, Z., & Forrest, D. (2012). The 2009 L'Aquila Mw 6.3 earthquake: A new technique to locate the hypocentre in the joint inversion of earthquake rupture process. *Geophysical Journal International*, *191*(3), 1417–1426.